RECENT *FUSE* OBSERVATIONS OF DIFFUSE O VI EMISSION FROM THE INTERSTELLAR MEDIUM[1]

W. Van Dyke Dixon

Department of Physics and Astronomy, Johns Hopkins University, 3400 N. Charles Street, Baltimore, MD 21218

AND

Ravi Sankrit[2]

Space Sciences Laboratory, University of California, Berkeley, CA 94720

To Appear in the Astrophysical Journal

ABSTRACT

We present new results from our survey of diffuse O VI-emitting gas in the interstellar medium with the *Far Ultraviolet Spectroscopic Explorer (FUSE).* Background observations obtained since 2005 have yielded eleven new O VI detections of 3σ significance, and archival searches have revealed two more. An additional 15 sight lines yield interesting upper limits. Combined with previous results, these observations reveal the large-scale structure of the O VI-bearing gas in the quadrant of the sky centered on the Magellanic Clouds. The most prominent feature is a layer of low-velocity O VI emission extending more than $70°$ from the Galactic plane. At low latitudes ($|b| < 30°$), the emission comes from narrow, high-density conductive interfaces in the local ISM. At high latitudes, the emission is from extended, low-density regions in the Galactic halo. We also detect O VI emission from the interface region of the Magellanic System, a structure recently identified from H I observations. These are the first detections of emission from high-ionization species in the Magellanic System outside of the Clouds themselves.

Subject headings: ISM: general — ISM: structure — Galaxy: structure — Magellanic Clouds — ultraviolet: ISM

1. INTRODUCTION

The lithium-like O VI ion is an important tool for studying hot gas in interstellar space, because emission via its 1031.93 and 1037.62 Å resonance lines is the dominant cooling mechanism for gas at temperatures of a few times 10^5 K (Gnat & Sternberg 2007). Recent O VI absorption-line surveys (Savage et al. 2003; Bowen et al. 2008) reveal that, within our Galaxy, the O VI-bearing gas has an exponential scale height of 3.2 kpc at negative latitudes and 4.6 kpc at positive latitudes. The gas is clumpy: spectra of nearly two dozen stars in the Large and Small Magellanic Clouds reveal significant variations in the O VI column density of Galactic halo gas over angular scales as small as $3\rlap{.}'5$ (Howk et al. 2002).

Closer to the plane, Bowen et al. (2008) find that the average volume density of O VI towards stars in the Galactic disk, $n = N(\text{O VI})/d$, exhibits a dispersion of about 0.26 dex, regardless of the distance to the target stars. They conclude that the O VI does not arise in randomly distributed clouds of a uniform size and density, but is instead distributed among regions with a broad range of column densities, with smaller clouds more common and larger clouds less so. They envision a turbulent, multiphase medium churned by shock-heated gas from multiple supernova explosions.

We present the latest results from a survey of diffuse O VI emission from the interstellar medium (ISM) conducted with the *Far Ultraviolet Spectroscopic Explorer (FUSE).* Otte & Dixon (2006, hereinafter Paper I) and

Dixon, Sankrit, & Otte (2006, Paper II) discuss observations obtained from launch through 2003 July 25 and 2004 December 31, respectively. In these papers, O VI emission at 3σ significance is detected along 29 lines of sight. Measured intensities range from 1.8 to 9.1 kLU, with a median of 3.3 kLU. An additional 35 sight lines provide upper limits of 2.0 kLU or less. (One line unit, or photon cm^{-2} s^{-1} sr^{-1}, corresponds to 1.9×10^{-11} erg cm^{-2} s^{-1} sr^{-1} at 1032 Å.) By combining emission and absorption measurements through the same O VI-bearing regions, the authors find evidence for two flavors of O VI-emitting gas: relatively narrow, high-density conductive interfaces in the local ISM and more extended, low-density regions in HVCs.

In this paper, we present data obtained between 2005 January 1 and 2007 July 6, along with two older observations that were missed in the earlier papers. In §2, we describe the *FUSE* instrument, our criteria for selecting sight lines for study, and our data-reduction and analysis techniques. In §3, we derive the physical parameters of the emitting gas and discuss its location along the line of sight. We present our conclusions in §4. Because the *FUSE* pointing system failed in July of 2007, these observations represent the final installment of our survey.

2. OBSERVATIONS, DATA REDUCTION, AND ANALYSIS

FUSE consists of four coaligned spectrographs. Two employ Al+LiF optical coatings and record spectra over the wavelength range 990–1187 Å, while the other two use SiC coatings, which provide reflectivity to wavelengths below the Lyman limit. The four channels overlap between 990 and 1070 Å. Each channel possesses three apertures that simultaneously sample different parts of the sky. The low-resolution (LWRS) aperture

Electronic address: wvd@pha.jhu.edu

is $30'' \times 30''$ in size. The medium-resolution (MDRS) aperture is $4'' \times 20''$ and lies about $3\rlap{.}'5$ from the LWRS aperture. The $1.25'' \times 20''$ high-resolution (HIRS) aperture lies midway between the MDRS and LWRS apertures. A fourth location, the reference point (RFPT), is offset from the HIRS aperture by about $1'$. When a star is placed at the reference point, all three apertures sample the background sky. For a complete description of *FUSE*, see Moos et al. (2000) and Sahnow et al. (2000).

To identify background observations for this study, we searched the Multimission Archive at Space Telescope (MAST) for *FUSE* data obtained after 2005 January 1 falling in one of three categories: programs S405, S505, S605, S705, and S905, which consist of background observations obtained during spacecraft thermalization periods; MDRS, HIRS, and RFPT observations of point sources, for which the LWRS aperture should sample only background sky; and targets whose names include the strings "BKG" or "SKY." To find older observations that may have been missed in our previous studies, we searched the entire archive for target names that include the strings "OFF," "SKY," or "WIND."

We exclude from our sample known supernova remnants, nebulae, and point-source targets in either of the Magellanic Clouds. Data from programs E124, G052, and G938 will be published elsewhere. Because its sensitivity at 1032 Å is more than twice that of any other channel, we consider only data from the LiF 1A channel. We use only data obtained in time-tag mode, which preserves arrival time and pulse-height information for each photon event. To avoid contamination by geocoronal emission (Shelton, Sallmen, & Jenkins 2007), we use only data obtained during orbital night. Individual exposures with less than 10 s of night exposure time are excluded from the survey, as are combined data sets with less than 1500 s of night exposure time or with significant continuum flux. Our final sample consists of data obtained along 120 lines of sight.

The data were reduced using an implementation of CalFUSE v3.2, the latest version of the *FUSE* data-reduction software package (Dixon et al. 2007), optimized for faint, diffuse emission. Details are given in Paper II, but we highlight a few points here: the program operates on one exposure at a time, producing a flux- and wavelength-calibrated spectrum from each. Background subtraction is turned off. Zero-point errors in the wavelength scale are corrected by fitting a synthetic emission feature to the Ly β airglow line. The spectra from individual exposures are then shifted to a heliocentric wavelength scale and combined.

We use an automated routine to search each combined spectrum for statistically significant emission near 1032 Å. When we find it, we fit the line with a model emission feature using the non-linear curve-fitting program SPECFIT (Kriss 1994). The model consists of a top-hat shaped function 106 km s^{-1} in width, representing the LWRS aperture, convolved with a Gaussian, representing the instrument line-spread function (~ 25 km s^{-1}) convolved with the intrinsic emission-line profile. Free parameters in the fit are the level and slope of the background (assumed linear) and the amplitude, central wavelength, and FWHM of the Gaussian.

While we use the same line identification and fitting algorithms described in Paper II, one change in our tech-nique is worth noting: Because our count rates are low, we bin the spectra to raise the counts per bin into the regime where Gaussian statistics apply. For most spectra, we bin by 14 pixels or 53 km s^{-1}, a value chosen so that that two binned pixels just span a diffuse emission feature. If the continuum averages more than 1.5 counts per pixel, we take advantage of the higher signal-to-noise ratio and bin by only 8 pixels. Because narrow emission features may be undersampled by 14-pixel binning, in Paper II we lowered the threshold for 8-pixel binning to 0.5 counts per bin for spectra containing features with FWHM < 100 km s^{-1}. In this paper, we use 14-pixel binning for all faint continua, regardless of the line width. Implications of this change are discussed below.

Our automated routine flags 32 spectra as having statistically significant O VI emission; i.e., the intensity of a putative emission feature is greater than 3 times the uncertainty in the local continuum. For only 13 of these spectra do model fits return line intensities with $I/\sigma(I) \geq 3$. We refer to these features as 3σ detections. Lines with $I/\sigma(I) < 3$ are referred to as 2σ detections. The best-fit parameters for both sets of O VI features are presented in Table 1, and plots of the spectra and best-fit models are presented in Figures 1 and 2. The asymmetric shapes of the narrowest model emission features are artifacts of our sparse sampling of the model lines.

Measured intensities range from 2.8 to 10.5 kLU, with a median of 4.0 kLU. Five of our 3σ detections have local standard of rest velocities $|v_{\mathrm{LSR}}| > 60$ km s^{-1}, while the rest have $|v_{\mathrm{LSR}}| < 35$ km s^{-1}. Four sight lines have FWHM values < 25 km s^{-1}, indicating that their O VI emission does not fill the LWRS aperture. For these sight lines, the surface brightness of the emitting region is underestimated and the velocity uncertain, as discussed in Paper II. For the non-detection sight lines, we compute 3σ upper limits to the intensity of an O VI emission feature using the mean background intensity between 1030 and 1035 Å and assuming a line width of 28 pixels (106 km s^{-1}). Upper limits for 15 sight lines with $I(\lambda 1032) \leq 2$ kLU are given in Table 2.

Four of our sight lines are previously published, but we include them here because additional data are now available. The original 26 ks observation of sight line B12901 is analyzed by Shelton (2003) and in Paper II. Recently, this line of sight was re-observed as target U10635, increasing the total exposure time to 40 ks. For this line of sight, an upper limit of 1.5 kLU is reported in Paper II (see their Table 6); our new upper limit is 1.2 kLU. Similarly, sight line C15301 was re-observed as target U10631, increasing the total exposure time from 93 to 102 ks. Our results (Table 1) are consistent with those of Shelton et al. (2007), who analyze the original C15301 data. A 5.2 ks observation of sight line S40577 was analyzed in Paper II, resulting in an upper limit of 3.6 kLU (see their Table 4). The total exposure time is now 24 ks, and our upper limit has fallen to 1.7 kLU.

Finally, a second observation of sight line S40590 has increased its exposure time from 10.8 to 15.2 ks. The measured flux is unchanged from that reported in Paper II, but the best-fit radial velocity has risen from -49 to -18 km s^{-1}. Part of this change may be attributed to the fact that, because the feature is so narrow, we binned the spectrum by 8 pixels in Paper II, while we bin it by 14 pixels for this paper. Binning the current

spectrum by 8 pixels yields a best-fit velocity of -29 ± 17 km s^{-1}. The larger problem is that the emission feature, with FWHM = 9 km s^{-1}, is unresolved, suggesting that the emitting region is smaller than the LWRS aperture. The uncertainty of its position within the aperture adds a systematic velocity uncertainty of about 50 km s^{-1}.

3. DISCUSSION

3.1. *Probing the Southern Galactic Sky*

Examination of Tables 1 and 2 reveals that most of the O VI detection sight lines in our sample lie in the region of the southern Galactic sky between $l = 180°$ and $360°$, while most of our upper limits lie in the region of the northern Galactic sky between $l = 0°$ and $180°$. The prominence of these two quadrants in the *FUSE* target list is discussed in Paper I and reflects observational constraints that reduced target availability in the orbit plane. The dearth of O VI detections among our northern sight lines may reflect their generally lower galactic latitudes, which are more likely to suffer significant extinction. Happily, the southern quadrant between $l = 180°$ and $360°$ is now reasonably well sampled in O VI emission, and we focus our attention there.

Figure 3 presents a map of the southern Galactic sky centered on the Magellanic Clouds. The background image is an H I map based on 21 cm emission measurements. Velocities are color-coded, with purple/blue representing negative velocities and orange/red representing positive velocities. Overplotted are large circles representing sight lines with significant high-velocity O VI absorption from the surveys of Sembach et al. (2003) and Wakker (in preparation). Their colors indicate the velocity of the absorbing gas using the same color scale as the H I emission. Small open circles indicate null detections. The large squares represent 3σ O VI detections from this survey and that of Paper II, also color-coded by velocity. Small open squares represent interesting upper limits ($I(\lambda 1032) \leq 2$ kLU) from both this survey and Paper II. For convenience, the O VI detections and limits taken from Paper II are reproduced in Tables 3 and 4.

Immediately apparent in Fig. 3 are the many sight lines exhibiting low-velocity O VI emission (green squares). Their wide distribution, extending to low galactic latitudes, suggests that they trace a larger structure (§3.2). Among the low-velocity sight lines are two that also exhibit O VI absorption (Fairall 9 and NGC 625), from which we can derive the physical parameters of the O VI-bearing gas (§3.4). Finally, the three sight lines showing high-velocity O VI emission (S70504, S90513, and I20505) allow us to probe the Magellanic System (§3.6).

3.2. *Comparing Low and High Latitudes*

In Paper II, we found evidence for two distinct flavors of O VI-emitting gas: relatively narrow (0.1 pc), high-density (0.1 cm^{-3}) conductive interfaces in the local ISM and more extended (100 pc), low-density (0.01 cm^{-3}) regions in high-velocity clouds. To look for evidence of this dichotomy within our current data set, we plot the measured O VI emission line intensity, line width, and velocity for the low-velocity 3σ emission features shown in Fig. 3 as a function of galactic latitude. The O VI intensities are plotted in Fig. 4. Overplotted is the color excess $E(B-V)$ along each line of sight (Schlegel, Finkbeiner, & Davis 1998). The figure includes a single sight line, S50508, with an O VI intensity of 9.1 kLU and a color excess $E(B-V) = 1.26$ (off scale). As discussed in Paper II, this sight line probes the outskirts of the Vela supernova remnant (250 pc distant). As it is not representative of the general ISM, we will not discuss it further.

The other sight lines fall into two groups: those at latitudes $|b| > 30°$, which suffer little reddening and whose intensities appear to fall with distance from the plane, and those with $|b| < 30°$, which suffer significant reddening. A color excess of $E(B-V) = 0.2$ corresponds to an attenuation factor of 14 (Fitzpatrick 1999), so it is unlikely that much of the absorbing material lies between us and the emitting gas. Either these low-latitude sight lines probe relatively nearby gas, or the extinction is patchy – or both.

The Gaussian FWHM values are plotted in Fig. 5. This parameter represents the combined effects of the instrumental line-spread function (~ 25 km s^{-1}) and the intrinsic velocity structure of the O VI-emitting gas. Though the uncertainties are large, the dichotomy between high- and low-latitude sight lines persists, with generally broad emission features at high latitudes and generally narrow features at low latitudes. It is striking that all four unresolved emission features (those with FWHM < 25 km s^{-1}, indicating that they do not fill the $30'' \times 30''$ LWRS aperture) lie at latitudes $|b| < 30°$. If their emitting regions lie within 1 kpc of the earth, then they have a maximum projected spatial extent of 0.15 pc, similar to the path lengths derived for conductive interfaces in the local ISM (Paper II). At temperatures near 3×10^5 K, thermal broadening would produce line widths of 40 km s^{-1} (after convolution with the *FUSE* line-spread function), so the broad emission features, more common at high latitudes, sample either turbulent gas or multiple emitting regions spanning a range of velocities.

The LSR velocities are plotted in Fig. 6. Grey bars represent the range of velocities predicted for each sight line by a simple model of Galactic rotation. Assuming a differentially-rotating halo with a constant velocity of $v = 220$ km s^{-1} and a distance from the sun to the Galactic center of 8.5 kpc, we compute the expected radial velocity as a function of distance for the first 5 kpc along each line of sight. The model ignores broadening due to turbulence or any other motion. While most of the low-latitude sight lines exhibit O VI velocities that are generally consistent with our model, most of the high-latitude sight lines do not. Instead, most are moving away from the Galactic plane at 10–30 km s^{-1}.

These trends are consistent with the picture derived in Paper II: that low-latitude sight lines tend to sample relatively small, dense regions in the local ISM, while high-latitude sight lines sample larger, lower-density, more turbulent regions farther from the disk. In the following two sections, we quantify the physical properties of these high-latitude emitting regions.

3.3. *O VI Column Density*

Figure 3 reveals O VI absorption and emission along two pairs of closely-spaced sight lines: toward the galaxies Fairall 9 and NGC 625. The Fairall 9 sight lines are more closely spaced. In an effort to observe O VI emission corresponding to the high-velocity O VI absorption

seen in the spectrum of Fairall 9 (Wakker et al. 2003), sight line D02401 was offset from the galaxy by about 1'. NGC 625 was observed in the usual way, with the galaxy in the MDRS aperture and the LWRS aperture observing the background sky some 3.'5 distant.

To measure the O VI column densities at velocities corresponding to their observed O VI emission, we obtained the fully-reduced *FUSE* spectra of both galaxies from MAST. When processing spectra from faint targets, the *FUSE* data-reduction pipeline runs CalFUSE (version 3.2.1) on each individual exposure, combines the data from all exposures into a single photon-event list, and extracts one spectrum for the whole observation. This technique maximizes the fidelity of the two-dimensional scattered-light model that is subtracted from the data. The resulting spectra are plotted in the top panels of Figs. 7 and 8. Both sight lines lie in the direction of the Magellanic Stream, and both spectra show O VI absorption extending to high velocities. Following Wakker et al. (2003), we choose 100 km s^{-1} as the dividing line between Galactic and Magellanic absorption.

We approximate an LSR velocity scale by shifting the spectra so that the interstellar Ar I $\lambda1048.2$ line falls at its laboratory wavelength, then fit a low-order polynomial to the continuum on either side of the O VI absorption. To account for absorption by molecular hydrogen, we scale the model continuum by a synthetic P(3) $\lambda1031.2$ absorption spectrum using the column densities, velocities, and line widths of Richter et al. (2001), Wakker (2006), and B. P. Wakker (2008, private communication). H$_2$ absorption is seen at velocities of -1 and 196 km s^{-1} toward Fairall 9 and 0 and 396 km s^{-1} toward NGC 625, as shown in the second panel of Figs. 7 and 8.

We derive O VI column densities using the apparent optical depth method (Savage & Sembach 1991), which is applicable when the spectral line to be measured is unsaturated and nearly resolved. The third panel of Figs. 7 and 8 shows the resulting column density N_a(O VI) as a function of velocity. (Note that N_a is plotted in units of cm^{-2} per velocity bin.) The resulting column densities for the low-velocity gas ($-110 < v < 100$ km s^{-1}) are $\log N = 14.38$ [cm^{-2}] toward Fairall 9 and $\log N = 14.50$ toward NGC 625. Our result for Fairall 9 is identical to that of Savage et al. (2003), though they do not correct for H$_2$ absorption in this spectrum.

The fourth panel of Figs. 7 and 8 reproduces the O VI emission spectrum for each sight line. In both cases, the peak of the O VI emission lines up nicely with the low-velocity component of the apparent column density N_a(O VI). We can quantify this alignment by computing the average LSR velocity of the Galactic O VI absorption ($-110 < v < 100$) using Equation 3 of Savage et al. (2003). For Fairall 9, $\bar{v} = 35$ km s^{-1}, consistent with the velocity (16 ± 21 km s^{-1}) of the emitting gas. (Savage et al. 2003 derive $\bar{v} = 24$ km s^{-1} over the same velocity range.) For NGC 625, $\bar{v} = 28$ km s^{-1}, again consistent with the velocity (19 ± 18 km s^{-1}) of the O VI emission.

3.4. *Physical Parameters of the High-Latitude Gas*

Measurements of O VI absorption and emission can be combined to provide valuable diagnostics of the O VI-bearing gas. Because the O VI column density is proportional to the density of the gas, while the line intensity is proportional to the density squared, the ratio of intensity to column density is proportional to the electron density in the emitting plasma.

The observed O VI $\lambda1032$ intensity toward Fairall 9 is 3.5 ± 1.1 kLU. We assume that the intrinsic intensity of the O VI $\lambda1038$ emission is half that of the 1032 Å line, as would be expected if the emitting gas were optically thin. The column density of the low-velocity ($-110 < v < 100$) O VI is $\log N = 14.38$. For an assumed temperature of 2.9×10^5 K, Equation 5 from Shull & Slavin (1994) yields an electron density $n_e = 9.5 \times 10^{-3}$ cm^{-3} and a thermal pressure $P/k = 1.92\,n_e T = 5300$ K cm^{-3}. The color excess toward Fairall 9 is $E(B-V) = 0.025$ (Schlegel et al. 1998), which attenuates emission at 1032 Å by $\sim 30\%$ (Fitzpatrick 1999). If all of that material lies between us and the emitting gas, n_e rises to 1.3×10^{-2} cm^{-3} and P/k to 7400 K cm^{-3}.

To calculate the O VI density and the path length through the emitting gas, we need the oxygen abundance and the fraction of oxygen in O^{+5}. From their sample of low-density ($\langle n_H \rangle < 1.0$ cm^{-3}) Galactic sight lines longer than 800 pc, Cartledge et al. (2004) derive a mean interstellar O/H ratio of $(4.37 \pm 0.09) \times 10^{-4}$. For plasmas in collisional ionization equilibrium, the O^{+5} fraction peaks at 21.5% when the gas temperature is 2.9×10^5 K (Gnat & Sternberg 2007). With these values, and assuming that the gas is completely ionized ($n_e = 1.2 n_H$), we derive an O VI density of 7.4×10^{-7} cm^{-3} and a path length through the gas of 100 pc for zero reddening. If $E(B-V) = 0.025$, then the O VI density and path length become 1.0×10^{-6} cm^{-3} and 75 pc, respectively.

The observed O VI $\lambda1032$ intensity toward NGC 625 is 2.6 ± 0.8 kLU and the column density of its low-velocity gas is $\log N = 14.50$. From these values, we derive an electron density for the O VI-bearing gas of $n_e = 5.3 \times 10^{-3}$ cm^{-3}, a thermal pressure $P/k = 3000$ K cm^{-3}, an O VI density of 4.2×10^{-7} cm^{-3}, and a path length through the emitting gas of 250 pc. The color excess toward NGC 625 is $E(B-V) = 0.016$, which attenuates emission at 1032 Å by $\sim 20\%$. Correcting for this attenuation raises the density and pressure and reduces the path length by the same factor.

Shelton et al. (2007) use shadowing arguments to conclude that essentially all of the O VI emission seen along sight line C15301 (at $l = 278.7, b = -47.1$ in Fig. 3) comes from the Galactic halo. Lacking a measurement of the O VI column density along this line of sight, they adopt an average of the published measurements for four nearby sight lines, $\log N = 14.37$, from which they derive an electron density $n_e = 1.1$–1.6×10^{-2} cm^{-3}, a thermal pressure $P/k = 7$–10×10^3 K cm^{-3}, and a path length of 50–70 pc for the emitting gas. These parameters are consistent with those derived from the Fairall 9 and NGC 625 data, suggesting a thick disk/halo origin for the O VI-emitting gas along all three lines of sight.

We can derive a lower limit to the distance of the O VI-emitting gas from the angular distance between a pair of O VI detection and upper-limit sight lines that are near one another on the sky. The two closest pairs are I20505/B12901 and C15301/Z90719, but both probe variations in the opacity of an intervening dust cloud (see the discussion in Appendix A2 of Paper II), rather than

variations in the intrinsic O VI emission. The third closest pair, C07601/S90522, is separated by $\sim 3°$. The non-detection of O VI along sight line S90522 is not due to interstellar opacity; the extinction maps of Schlegel et al. (1998) suggest that it is less affected by dust than is C07601. If the O VI-emitting region sampled by sight line C07601 has a radius of ~ 100 pc (assuming size $\sim$ path length), then it lies at least 2 kpc from the Sun and at least 800 pc from the Galactic plane.

3.5. *Comparison with Models*

A successful model of the hot component of the interstellar medium must reproduce our observational results: Diffuse O VI emission (i.e., emission unrelated to discrete supernova remnants or superbubbles) is present over the entire sky with intensities between about 2 and 6 kLU. The emission is patchy: of the sight lines providing statistically-significant results, roughly 40% yield upper limits $I(\text{O VI}) < 2$ kLU. Near the plane, the emitting regions are less than about 0.15 pc in spatial extent, with electron densities $n_e = 0.2 - 0.3$ cm^{-3} (Paper II). At high latitudes, the emitting regions are large, with path lengths on the order of 100 pc, and at least 800 kpc from the plane. Electron densities are on the order of 10^{-2} cm^{-3}

In a series of papers, de Avillez & Breitschwerdt (2004, 2005a,b) present the results of high-resolution, three-dimensional hydrodynamic and magnetohydrodynamic simulations of the ISM. The authors model a section of the Galaxy centered on the solar circle having an area of 1 kpc^2 and extending ± 10 kpc from the Galactic plane. They employ an adaptive mesh refinement algorithm whose resolution peaks at 1.25 pc within the disk ($|z| \leq 500$ pc). By computing $N(\text{O VI})$ along hundreds of sight lines (all with $|z| \leq 250$ pc and $d \leq 1$ kpc) through their data cube, de Avillez & Breitschwerdt (2005b) are able to reproduce both the observed distribution of $N(\text{O VI})$ with distance and its dispersion.

We derive electron densities $n_e \sim 10^{-2}$ cm^{-3} for the O VI-emitting gas along the lines of sight toward Fairall 9 and NGC 625. de Avillez & Breitschwerdt (2005a, see their Fig. 2) present a two-dimensional vertical slice (perpendicular to the midplane) through their three-dimensional data cube showing the density distribution of the ISM. Gas parcels with densities on the order of 10^{-2} cm^{-3} are present throughout the frothy thick disk of ionized and neutral gas lofted by supernova explosions in the plane. The boundaries of these parcels would be natural locations for the formation of O VI-bearing interfaces. Model predictions of $N(\text{O VI})$ and $I(\text{O VI})$ as functions of Galactic latitude have not yet been published.

3.6. *O VI Emission from the Magellanic System*

The three sight lines in Fig. 3 with high-velocity O VI emission are S70504 ($+84$ km s^{-1}) and S90513 ($+115$ km s^{-1}) from the current sample and I20505 ($+206$ km s^{-1}) from Paper II. All three lie in a region of the Magellanic System designated as the "interface region" by Brüns et al. (2005, see their Fig. 4). The interface region connects the Magellanic Clouds and the Magellanic Bridge with the Magellanic Stream, which lies to the south of $-60°$ latitude. The H I in this region exhibits a complex filamentary structure and a distinct velocity

signature. Sight lines S90513 and I20505 lie near the projected western and eastern edges of the region, respectively, and the observed LSR velocities of their O VI emission closely match those of the H I. Although the O VI velocity along sight line S70504 is about half that of the H I in the same direction, it is within the overall range of H I velocities detected in the interface region, 60–360 km s^{-1}.

The interface region of the Magellanic System lies about 40 kpc from the Galactic plane (Jin & Lynden-Bell 2008) and is thus embedded in the hot (10^6 K) Galactic corona. The perimeters of these high-velocity H I clouds, where cool and hot gas meet and mingle, are natural sites for the formation of intermediate-temperature O VI-bearing gas. Indeed, Sembach et al. (2003) report O VI absorption along several extragalactic sight lines (including Fairall 9) that probe the Magellanic Stream at velocities consistent with that of the H I gas. Intriguingly, while both Fairall 9 and NGC 625 show O VI absorption at Magellanic velocities, neither shows high-velocity O VI emission. The interface region, which does show O VI emission, is unique in this respect.

These are the first detections of high-ionization emission from the Magellanic System outside of the Clouds themselves. The O VI intensities observed along the two sight lines towards the edges of the interface region are well within the normal range observed in the diffuse ISM, but the intensity along sight line S70504 (10.5 kLU) is significantly higher. In fact, it is the highest diffuse O VI intensity observed to date (outside of supernova remnants, superbubbles, and high-ionization planetary nebulae). Though the O VI emission feature in this spectrum is statistically significant, its exposure time is quite short, just over 2 ks. Deeper and more detailed observations would help to determine whether such high intensities are commonly obtained in the interface region of the Magellanic System.

4. CONCLUSIONS

We present the final installment of the *FUSE* survey of diffuse O VI emission in the interstellar medium. These observations reveal the large-scale structure of the O VI-bearing gas in the quadrant of the sky centered on the Magellanic Clouds. Its most prominent feature, a layer of low-velocity O VI emission extending more than $70°$ from the Galactic plane, is produced by two distinct populations of emitting clouds. At latitudes $|b| < 30°$, sight lines suffer significant extinction, suggesting that they probe relatively nearby emitting regions; their emission features are more likely to be narrow or unresolved, suggesting single interfaces less than about 0.15 pc across; and their velocities are generally consistent with Galactic rotation. We identify these emitting regions with narrow, high-density interfaces in the local ISM.

At latitudes $|b| > 30°$, extinction is low. Intensities fall with distance from the plane. Emission features are generally broad, suggesting that they sample turbulent gas or multiple emitting regions spanning a range of velocities. The O VI-bearing gas seems to be moving away from the Galactic plane. For two sight lines, Fairall 9 and NGC 625, we combine O VI-emission and -absorption measurements to constrain the physical parameters of the emitting regions. From the resulting path lengths, we estimate that these regions lie at least 800 pc from

the Galactic plane. The presence of nearby sight lines yielding null detections but strong upper limits suggests that the emission is patchy, consistent with the results of Howk et al. (2002).

High-velocity O VI emission is seen along three sight lines that probe the interface region of the Magellanic System. The O VI velocities are generally consistent with those of the underlying H I. High-velocity O VI emission is not seen in sight lines that probe the Magellanic Stream, suggesting that the dynamics of the interface region differ from those of the Stream itself. These are the first detections of emission from high-ionization species in the Magellanic System outside of the Clouds themselves.

REFERENCES

Bowen, D. V. et al. 2008, ApJS, 176, 59
Brüns, C. et al. 2005, A&A, 432, 45
Cartledge, S. I. B., Lauroesch, J. T., Meyer, D. M., & Sofia, U. J. 2004, ApJ, 613, 1037
de Avillez, M. A. & Breitschwerdt, D. 2004, A&A, 425, 899
—. 2005a, A&A, 436, 585
—. 2005b, ApJ, 634, L65
Dixon, W. V., Sankrit, R., & Otte, B. 2006, ApJ, 647, 328
Dixon, W. V. et al. 2007, PASP, 119, 527
Fitzpatrick, E. L. 1999, PASP, 111, 63
Gnat, O. & Sternberg, A. 2007, ApJS, 168, 213
Howk, J. C., Savage, B. D., Sembach, K. R., & Hoopes, C. G. 2002, ApJ, 572, 264
Hulsbosch, A. N. M. & Wakker, B. P. 1988, A&AS, 75, 191
Jin, S. & Lynden-Bell, D. 2008, MNRAS, 383, 1686
Kriss, G. A. 1994, in ASP Conf. Ser. 61, Astronomical Data Analysis Software and Systems III, ed. D. R. Crabtree, R. J. Hanisch, & J. Barnes (San Francisco: ASP), 437
Moos, H. W. et al. 2000, ApJ, 538, L1

Morras, R., Bajaja, E., Arnal, E. M., & Pöppel, W. G. L. 2000, A&AS, 142, 25
Otte, B. & Dixon, W. V. 2006, ApJ, 647, 312
Richter, P., Sembach, K. R., Wakker, B. P., & Savage, B. D. 2001, ApJ, 562, L181
Sahnow, D. J. et al. 2000, ApJ, 538, L7
Savage, B. D. & Sembach, K. R. 1991, ApJ, 379, 245
Savage, B. D. et al. 2003, ApJS, 146, 125
Schlegel, D. J., Finkbeiner, D. P., & Davis, M. 1998, ApJ, 500, 525
Sembach, K. R. et al. 2003, ApJS, 146, 165
Shelton, R. L. 2003, ApJ, 589, 261
Shelton, R. L., Sallmen, S. M., & Jenkins, E. B. 2007, ApJ, 659, 365
Shull, J. M. & Slavin, J. D. 1994, ApJ, 427, 784
Wakker, B. P. 2006, ApJS, 163, 282
Wakker, B. P. et al. 2003, ApJS, 146, 1

TABLE 1
O VI λ1032 Detections

Sight Line	Target Name[a]	l (deg)	b (deg)	t[b] (s)	Bin[c]	Intensity[d] (kLU)	Wavelength[e] (Å)	FWHM[f] (km s^{-1})	v_{LSR} (km s^{-1})	$E(B-V)$[g] (mag)
					3σ Detections					
C15301[h]	SKY-032010-622629	278.7	−47.1	102371	8	3.5 ± 0.6	1032.02 ± 0.05	150 ± 20	12 ± 14	0.025
D02401	FAIRALL9-OFF	295.1	−57.8	28325	8	3.5 ± 1.1	1032.02 ± 0.07	120 ± 70	17 ± 21	0.025
S40590	HE2-138-BKGD	319.7	−9.4	15165	14	3.3 ± 0.8	1031.88 ± 0.04	9 ± 50	−18 ± 11	0.109
S50550	BKGD	280.7	−13.9	18453	8	2.8 ± 0.9	1031.90 ± 0.07	60 ± 20	−22 ± 20	0.145
S50553	BKGD	276.1	−22.4	13595	14	2.9 ± 0.8	1032.04 ± 0.04	9 ± 240	18 ± 13	0.117
S50557	BKGD	275.9	−37.5	7815	14	5.1 ± 1.6	1031.94 ± 0.06	50 ± 80	−13 ± 19	0.036
S50597	BKGD	317.3	−6.2	15359	8	6.5 ± 2.0	1031.36 ± 0.08	140 ± 60	−168 ± 25	0.420
S60588	NBKGD88	91.6	18.7	33917	8	3.4 ± 1.0	1031.66 ± 0.08	180 ± 60	−61 ± 23	0.068
S70504	SBKGD4	288.8	−49.4	2223	14	10.5 ± 3.1	1032.26 ± 0.05	20 ± 90	84 ± 14	0.024
S70512	SBKGD12	279.5	−14.9	11214	14	6.9 ± 2.0	1031.75 ± 0.07	140 ± 60	−65 ± 22	0.151
S70514	SBKGD14	286.0	−7.8	19190	14	4.0 ± 1.2	1032.04 ± 0.06	100 ± 50	22 ± 19	0.255
S90513	SBKGD	312.7	−47.6	8609	14	5.5 ± 1.2	1032.35 ± 0.02	2 ± 20	116 ± 6	0.028
S90523	SBKGD23A	320.8	−40.7	8045	14	5.1 ± 1.7	1032.01 ± 0.06	50 ± 80	19 ± 16	0.028
					2σ Detections					
G08101	HD128620	315.7	−0.7	5717	14	5.7 ± 2.3	1030.92 ± 0.06	6 ± 80	−295 ± 18	6.505
S50573	BKGD	288.0	−6.6	1918	14	20.3 ± 8.9	1032.07 ± 0.32	480 ± 150	29 ± 94	0.369
S50574	POLE-174-BKG	323.1	−45.8	4738	14	7.9 ± 4.4	1031.54 ± 0.25	300 ± 80	−118 ± 73	0.025
S50577	POLE-177-BKG	328.9	−39.6	5490	14	4.8 ± 1.8	1033.61 ± 0.06	2 ± 600	485 ± 17	0.032
S50578	POLE-178-BKG	329.7	−37.1	5736	14	5.3 ± 2.5	1032.11 ± 0.13	140 ± 80	49 ± 39	0.038
S50594	BKGD	129.6	15.9	8266	14	2.4 ± 1.2	1032.62 ± 0.08	30 ± 60	210 ± 23	0.285
S60514	NBKGD14	146.2	43.7	7341	14	5.2 ± 2.1	1033.35 ± 0.15	200 ± 50	418 ± 43	0.050
S70501	SBKGD1	311.6	−51.2	3487	14	4.1 ± 2.2	1032.85 ± 0.08	20 ± 140	259 ± 24	0.019
S70509	SBKGD9	274.6	−28.7	14400	14	2.1 ± 1.3	1032.40 ± 0.09	7 ± 200	121 ± 27	0.064
S70516	SBKGD16	294.9	−3.3	8219	14	3.5 ± 1.4	1031.59 ± 0.06	20 ± 270	−109 ± 18	1.260
S70522	SBKGD22	322.2	−9.9	23374	14	1.4 ± 0.6	1031.65 ± 0.03	3 ± 30	−82 ± 10	0.137
S70527	SBKGD27	331.2	−32.0	8016	14	7.8 ± 3.8	1032.42 ± 0.17	200 ± 90	141 ± 49	0.087
S70528	SBKGD28	330.4	−36.7	15182	8	2.9 ± 1.2	1034.03 ± 0.05	6 ± 30	607 ± 14	0.039
S70540	SBKGD40	281.8	−21.6	2820	14	8.3 ± 3.9	1033.21 ± 0.08	20 ± 210	357 ± 24	0.176
S70549	SBKGD49	318.6	−13.5	3081	14	4.2 ± 2.6	1031.92 ± 0.09	10 ± 220	−5 ± 26	0.106
S70567	SBKGD67	268.8	−30.6	2001	14	5.7 ± 3.6	1030.92 ± 0.08	4 ± 80	−309 ± 24	0.051
S70569	SBKGD69	270.7	−21.0	5650	14	4.8 ± 2.3	1034.09 ± 0.07	10 ± 230	611 ± 19	0.131
S90510	SBKGD10A	274.3	−20.4	3445	14	6.8 ± 2.9	1032.30 ± 0.07	5 ± 90	93 ± 21	0.138
S90524	SBKGD24A	278.5	−54.3	8968	14	3.1 ± 1.2	1031.96 ± 0.07	20 ± 80	−4 ± 19	0.030

[a] Target names are taken from the data file headers. [b] Exposure time is night only. [c] Spectral binning in 0.013 Å pixels. [d] kLU = 1000 photon s^{-1} cm^{-2} sr^{-1}. [e] Wavelengths are heliocentric. [f] Gaussian FWHM values include the smoothing imparted by the instrument optics. Values less than ∼ 25 km s^{-1} indicate that the emission does not fill the LWRS aperture. [g] Extinction from Schlegel et al. 1998. [h] Combines data sets C15301 and U10631. See discussion in text.

TABLE 2
3σ Upper Limits on O VI λ1032 Emission

Sight Line	Target Name[a]	l (deg)	b (deg)	t[b] (s)	3σ Limit[c] (kLU)	$E(B-V)$[d] (mag)
A15101	IPM-Upwind	3.7	18.5	24140	1.6	0.853
B12901[e]	SKY-033255-632751	278.6	−45.3	39983	1.2	0.160
S40577[f]	HDE232522-BKGD	130.7	−6.7	24329	1.7	0.278
S50551	BKGD	277.6	−17.7	30521	1.6	0.172
S50589	POLE-BKG	308.5	−8.9	33483	1.5	0.268
S60503	NBKGD3	27.3	2.5	27071	1.5	2.436
S60504	NBKGD4	132.0	3.7	31556	1.4	1.159
S60507	NBKGD7	144.1	11.9	19715	1.8	0.512
S60537	NBKGD37	140.6	15.6	22511	1.7	0.199
S60538	NBKGD38	143.3	19.8	27384	1.6	0.108
S60563	NBKGD63	140.0	2.0	14849	2.0	1.984
S60565	NBKGD65	147.6	8.2	23516	1.6	0.662
S70502	SBKGD2	303.8	−51.7	18927	1.8	0.019
S80502	NBKGD02	90.7	21.0	10074	2.0	0.074
S90522	SBKGD22A	333.3	−26.7	20974	2.0	0.047

[a] Target names are taken from the data file headers.[b] Exposure time is night only.[c] kLU = 1000 photon s^{-1} cm^{-2} sr^{-1}.[d] Extinction from Schlegel et al. 1998.[e] Combines data sets B12901 and U10635. See discussion in text.[f] Includes data from observation S4057701, obtained in 2002.

TABLE 3
3σ Detections of O VI λ1032 Emission near the Magellanic Clouds from Paper II

Sight Line	Target Name[a]	l (deg)	b (deg)	t[b] (s)	Bin[c]	Intensity[d] (kLU)	Wavelength[e] (Å)	FWHM[f] (km s^{-1})	v_{LSR} (km s^{-1})	$E(B-V)$[g] (mag)
C07601	NGC6752	336.5	−25.6	56225	8	1.8 ± 0.4	1031.87 ± 0.02	6 ± 10	−17 ± 6	0.056
C10503	MS2318.2-4220	348.1	−66.3	97954	8	1.8 ± 0.4	1031.92 ± 0.05	90 ± 40	−5 ± 13	0.021
D04001	NGC625	273.7	−73.1	43428	8	2.6 ± 0.8	1032.03 ± 0.06	90 ± 50	19 ± 18	0.016
D90305	Fairall 917	346.6	−39.5	21796	14	5.5 ± 1.5	1031.96 ± 0.08	180 ± 50	11 ± 24	0.035
I20505[h]	DET-BKGND	278.6	−45.3	46386	8	3.0 ± 0.6	1032.69 ± 0.05	100 ± 20	206 ± 13	0.160
I20509	Background	315.0	−41.3	93437	8	3.3 ± 0.6	1032.05 ± 0.05	170 ± 40	26 ± 16	0.036
P10411	WD0455-282	229.3	−36.2	46240	8	4.3 ± 0.9	1031.95 ± 0.03	60 ± 40	−12 ± 9	0.023
P20422	WD2004-605	336.6	−32.9	76972	8	4.8 ± 0.6	1031.91 ± 0.03	130 ± 30	−7 ± 8	0.049
P20516	LSE 44	313.4	13.5	85811	8	3.5 ± 0.6	1031.83 ± 0.04	100 ± 20	−28 ± 12	0.124
S40506	HD093840-BKGD	282.1	11.1	12962	8	4.0 ± 1.3	1031.91 ± 0.05	20 ± 100	−14 ± 13	0.167
S50508	LS982-BKGD	257.1	−3.9	10515	8	9.1 ± 1.8	1031.97 ± 0.03	30 ± 30	−4 ± 8	1.260

[a] Target names are taken from the data file headers.[b] Exposure time is night only.[c] Spectral binning in 0.013 Å pixels.[d] 1 LU = 1 photon s^{-1} cm^{-2} sr^{-1}.[e] Wavelengths are heliocentric.[f] Gaussian FWHM values include the smoothing imparted by the instrument optics. Values less than ∼ 25 km s^{-1} indicate that the emission does not fill the LWRS aperture.[g] Extinction from Schlegel et al. 1998.[h] See Table 6 of Paper II.

TABLE 4
Upper Limits (≤ 2.0 kLU) on O VI λ1032 Emission near the Magellanic Clouds from Paper II

Sight Line	Target Name[a]	l (deg)	b (deg)	t[b] (s)	3σ Limit[c] (kLU)	$E(B-V)$[d] (mag)
D90302	IRAS03335-5626	269.4	−48.9	33946	1.5	0.025
P10425	HD128620/HD128621	315.7	−0.7	26651	1.6	6.505
P20406	WD2127-222	27.4	−43.8	18938	2.0	0.046
S10102	WD1634-573	329.9	−7.0	67118	1.2	0.342
S40573	HD35580-BKGD	264.2	−34.5	40611	1.3	0.040
S40582	CD-61_1208-BKGD	270.1	−30.6	42039	1.2	0.052
S52301	WD2211-495-BKGD	345.8	−52.6	58547	1.2	0.015
Z90702	CTS0563	354.7	−49.9	15329	1.5	0.017
Z90719	ESO116-G18	276.2	−47.6	10485	2.0	0.075
Z90737	FAIRALL333	327.7	−23.8	29366	1.4	0.083

[a] Target names are taken from the data file headers.[b] Exposure time is night only.[c] 1 LU = 1 photon s^{-1} cm^{-2} sr^{-1}.[d] Extinction from Schlegel et al. 1998.
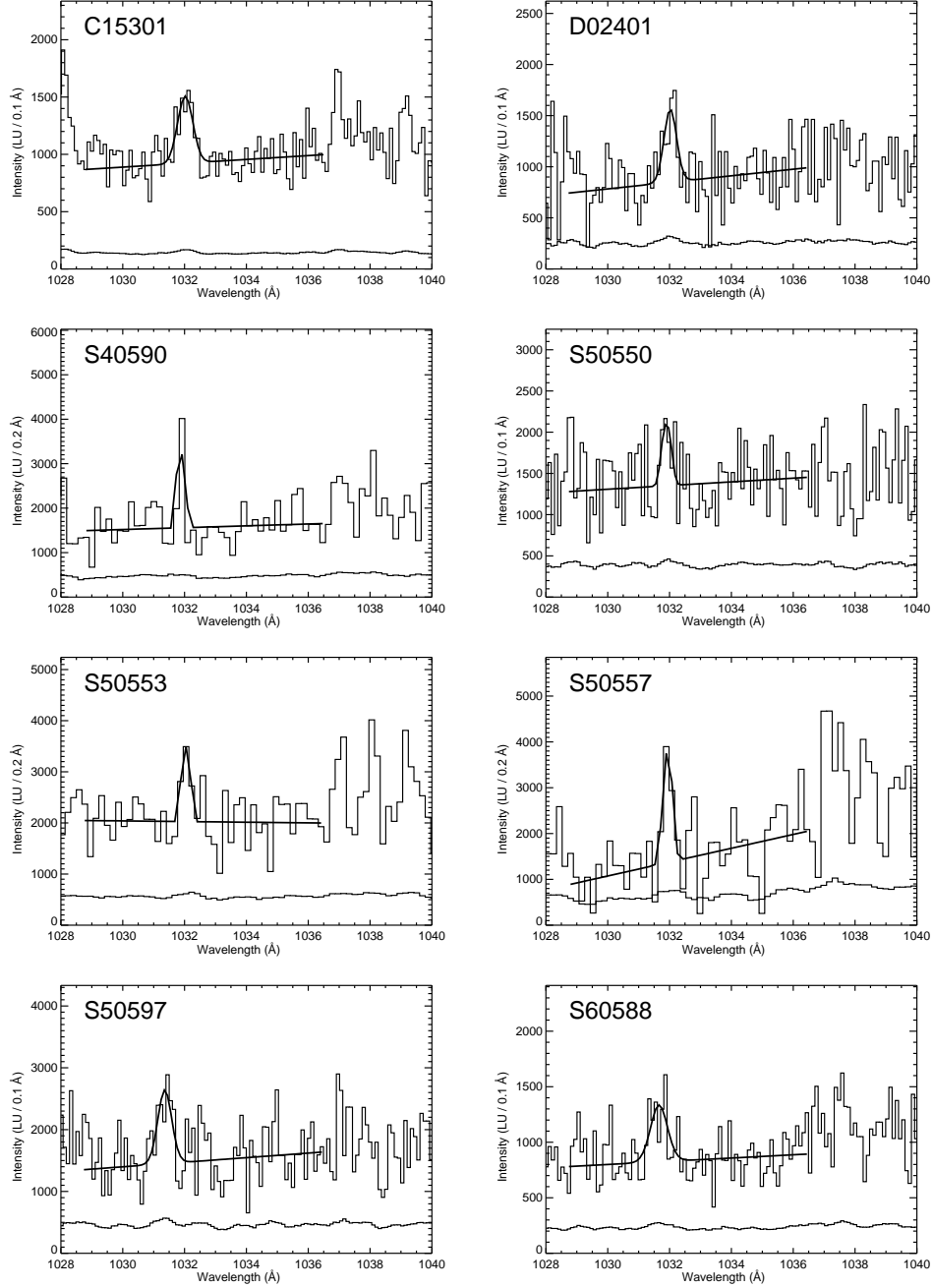
FIG. 1.— High-significance (3σ) O VI λ1032 emission features. The data are binned by the factors given in Table 1, and best-fit model spectra and error bars are overplotted. Interstellar C II* λ1037 and O VI λ1038 are present in some spectra, as are the geocoronal O I $\lambda\lambda$1028, 1039 lines.
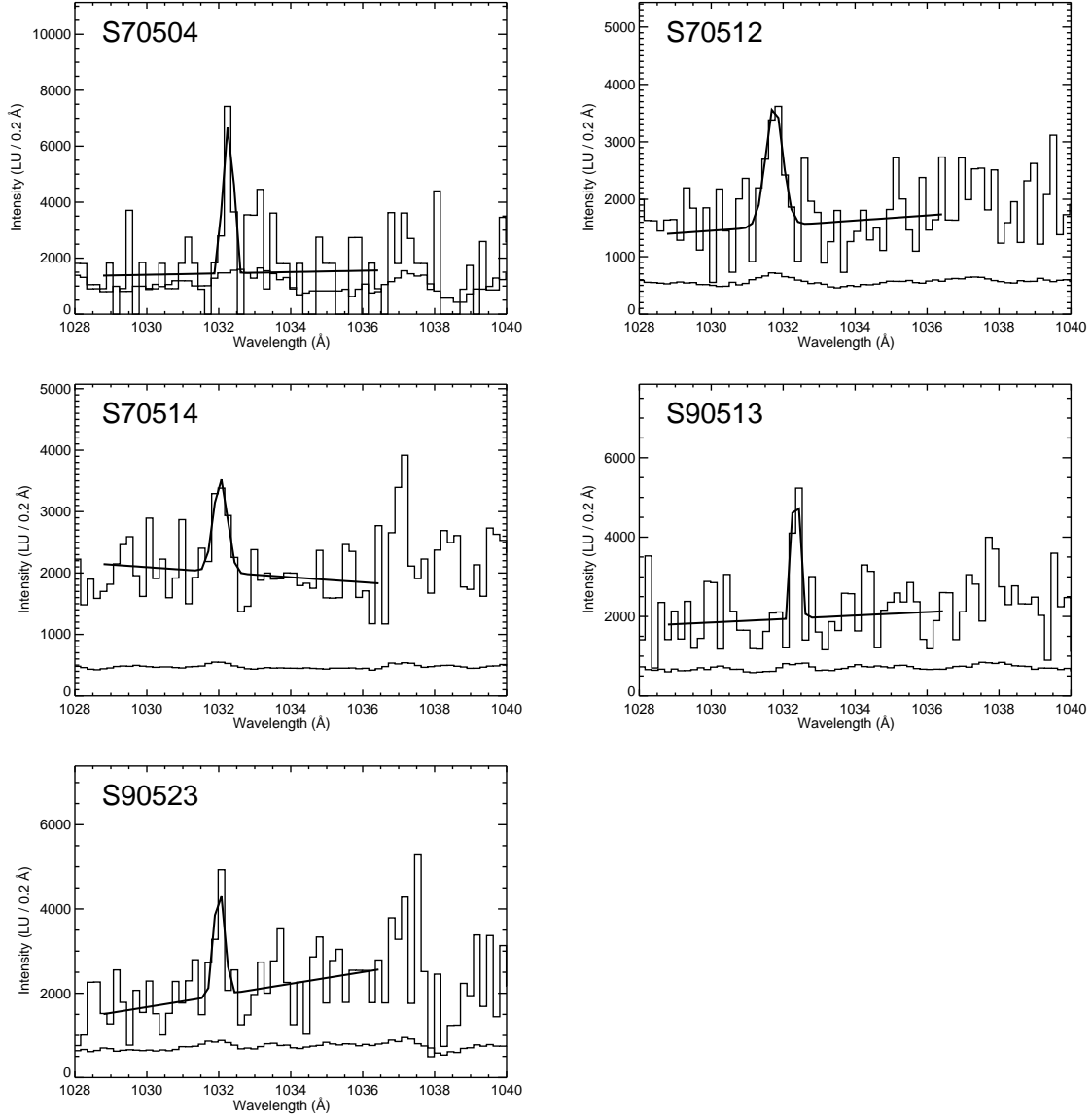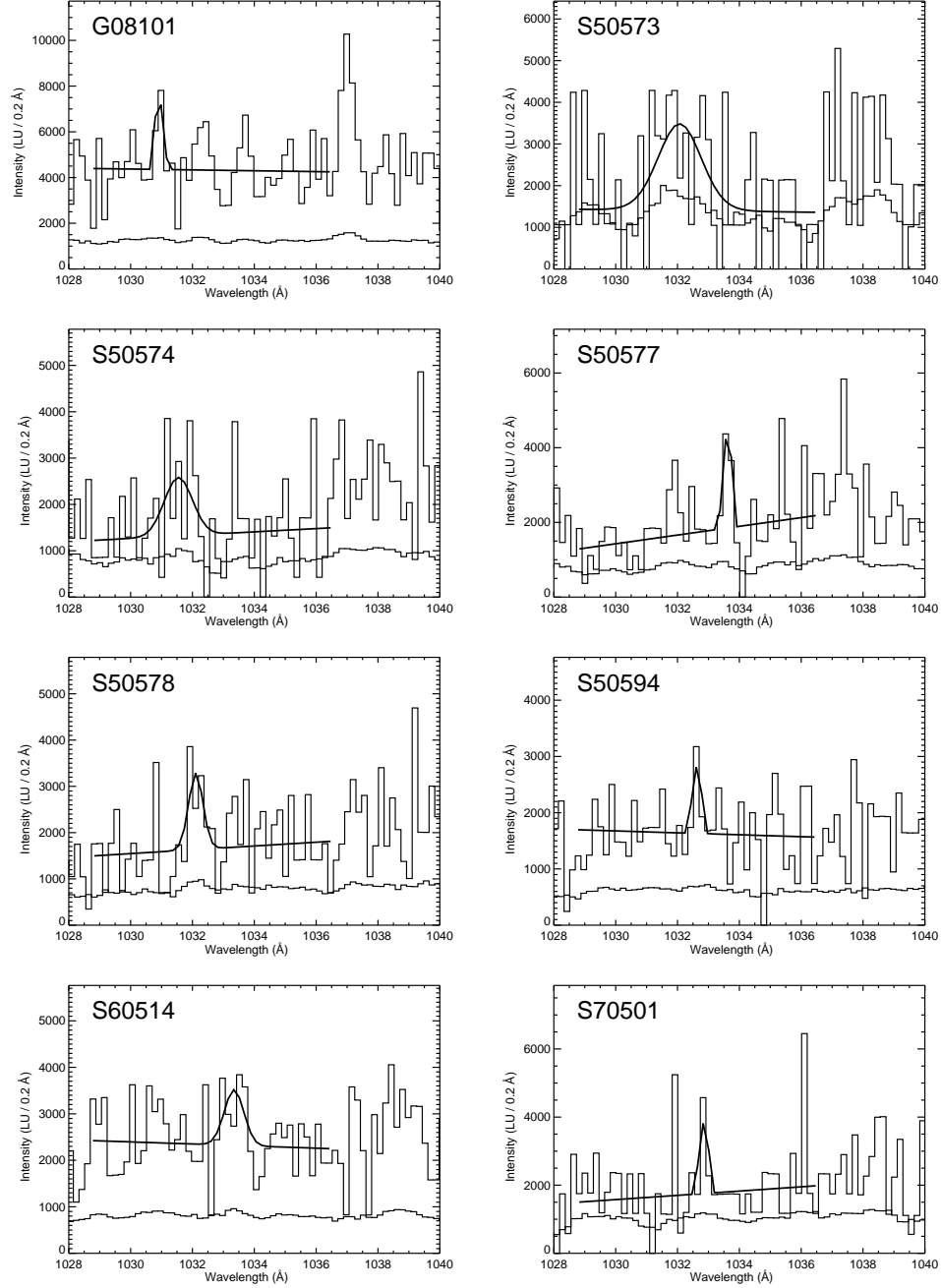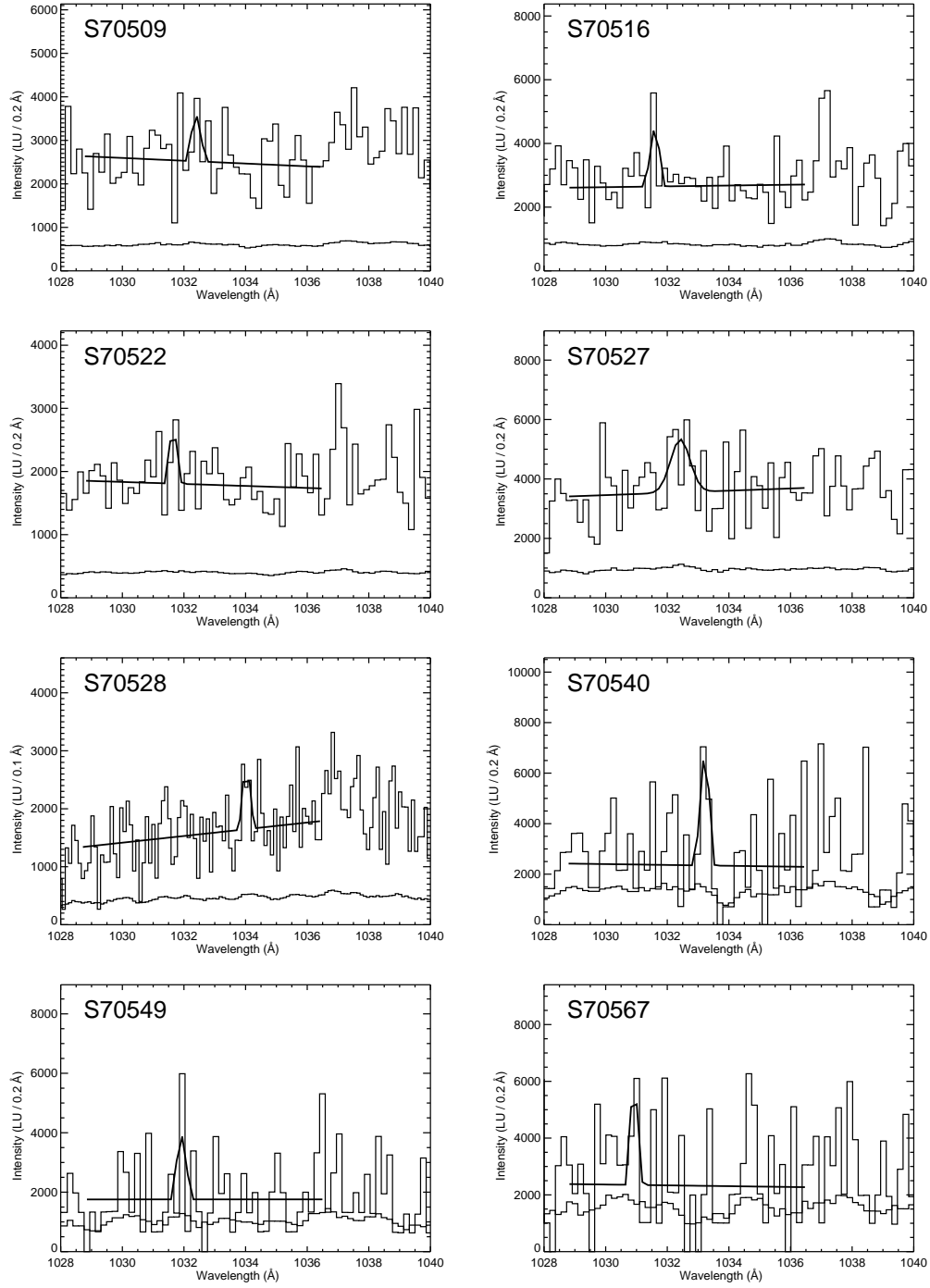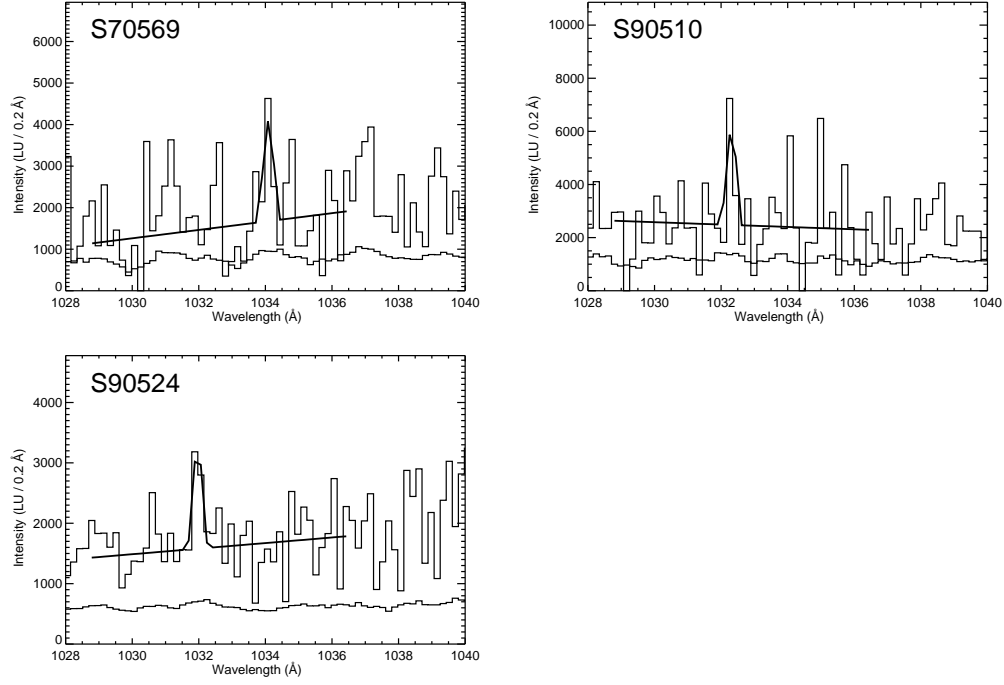
Fig. 1. — Continued.

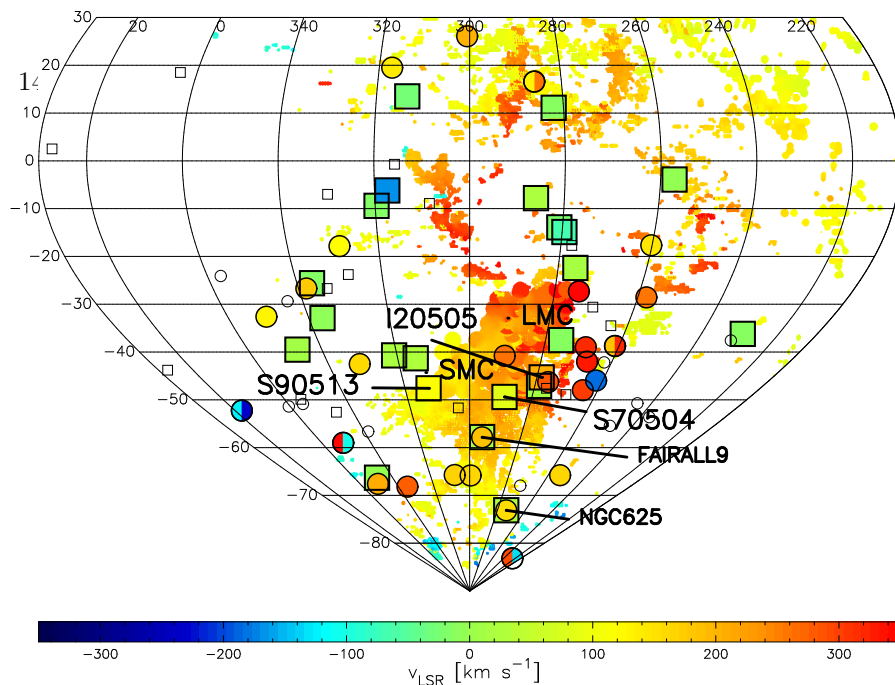FIG. 2.— Low-significance (2σ) O VI λ1032 emission features. The data are binned by the factors given in Table 1, and best-fit model spectra and error bars are overplotted. Interstellar C II* λ1037 and O VI λ1038 are present in some spectra, as are the geocoronal O I $\lambda\lambda$1028, 1039 lines.

Fig. 2. — Continued.

Fig. 2. — Continued.

FIG. 3.— Hammer-Aitoff projection of the high-velocity H I sky based on the 21 cm emission measurements of Morras et al. (2000) and Hulsbosch & Wakker (1988). The H I data have a spatial resolution of approximately $36'$ and are representative of gas with $N(\text{H I})$ $> 2 \times 10^{18}$ cm^{-2}. The map is centered on the Magellanic Clouds; coordinates are galactic longitude and latitude. Positions of the high-velocity O VI absorption features reported in Sembach et al. (2003) and Wakker (in preparation) are indicated by the large circles, whose colors indicate velocity on the same color scale used for the H I emission. If more than one high-velocity O VI absorption feature is present along a line of sight, the circle is split and the velocities are color-coded in each section of the circle. Small open circles indicate null detections. Positions of the O VI emission features reported in this paper and in Paper II are indicated by large squares, also color-coded by velocity. Small squares represent upper limits ≤ 2 kLU. Labeled sight lines are discussed in the text.
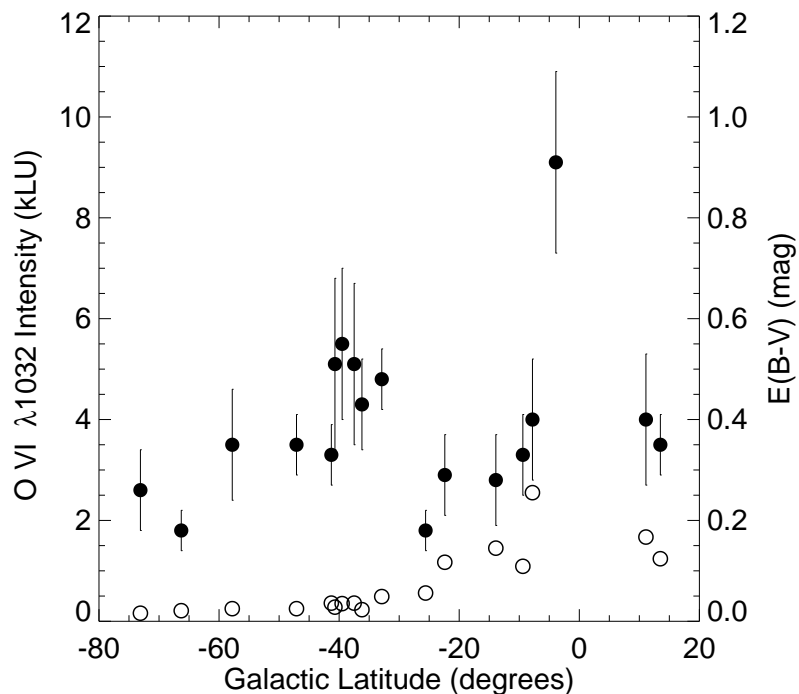

FIG. 4.— Variation of observed O VI $\lambda1032$ intensity with galactic latitude. Solid circles represent the low-velocity ($|v_{\text{LSR}}| < 60$ km s^{-1}) 3σ detections from Fig. 3. Open circles represent the color excess $E(B-V)$ along each line of sight. Note that the color excess is scaled by a factor of ten relative to intensity.
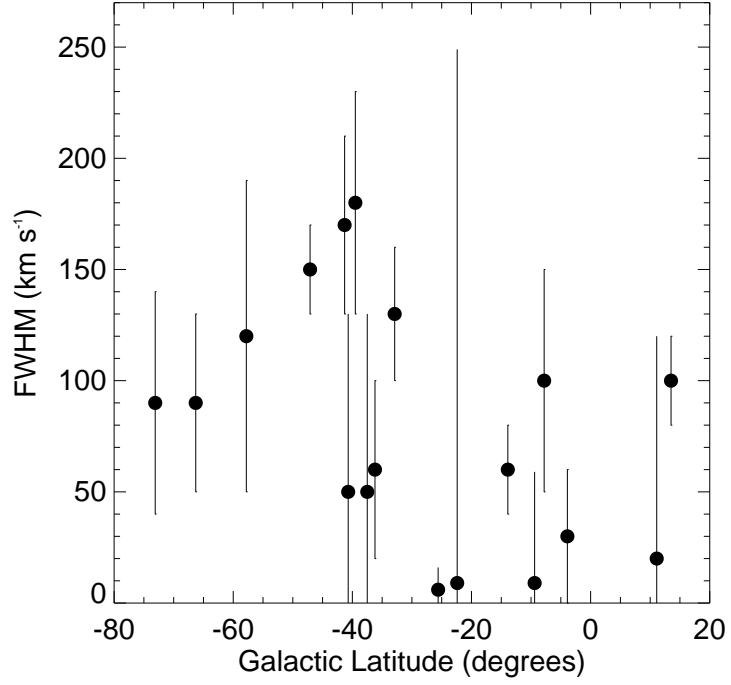
FIG. 5.— Best-fit Gaussian FWHM value as a function of galactic latitude. Solid circles represent the low-velocity ($|v_{\mathrm{LSR}}| < 60$ km s^{-1}) 3σ detections from Fig. 3.

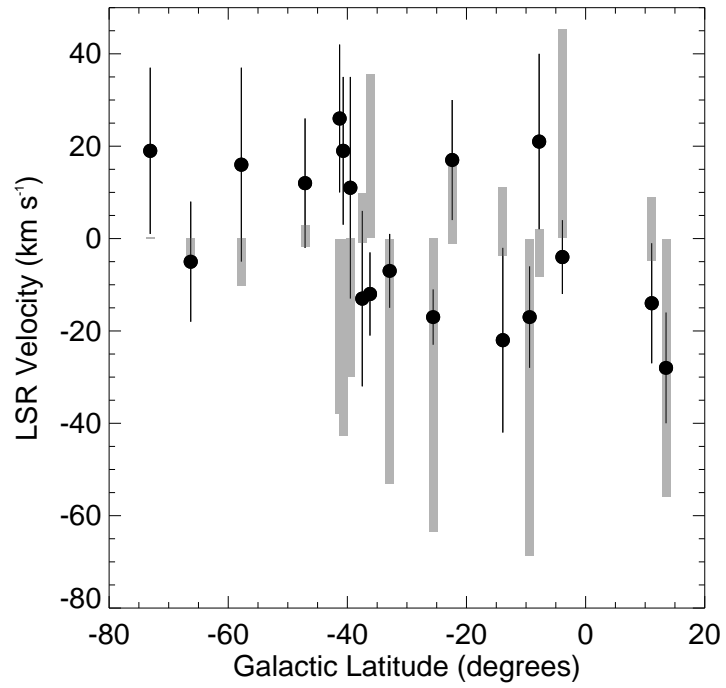FIG. 6.— Variation of LSR velocity with galactic latitude. Solid circles represent the low-velocity ($|v_{\mathrm{LSR}}| < 60$ km s^{-1}) 3σ detections from Fig. 3. Grey bars represent the range of LSR velocities predicted for the first 5 kpc along each sight line by a simple (cylindrical, constant-velocity) model of Galactic rotation.
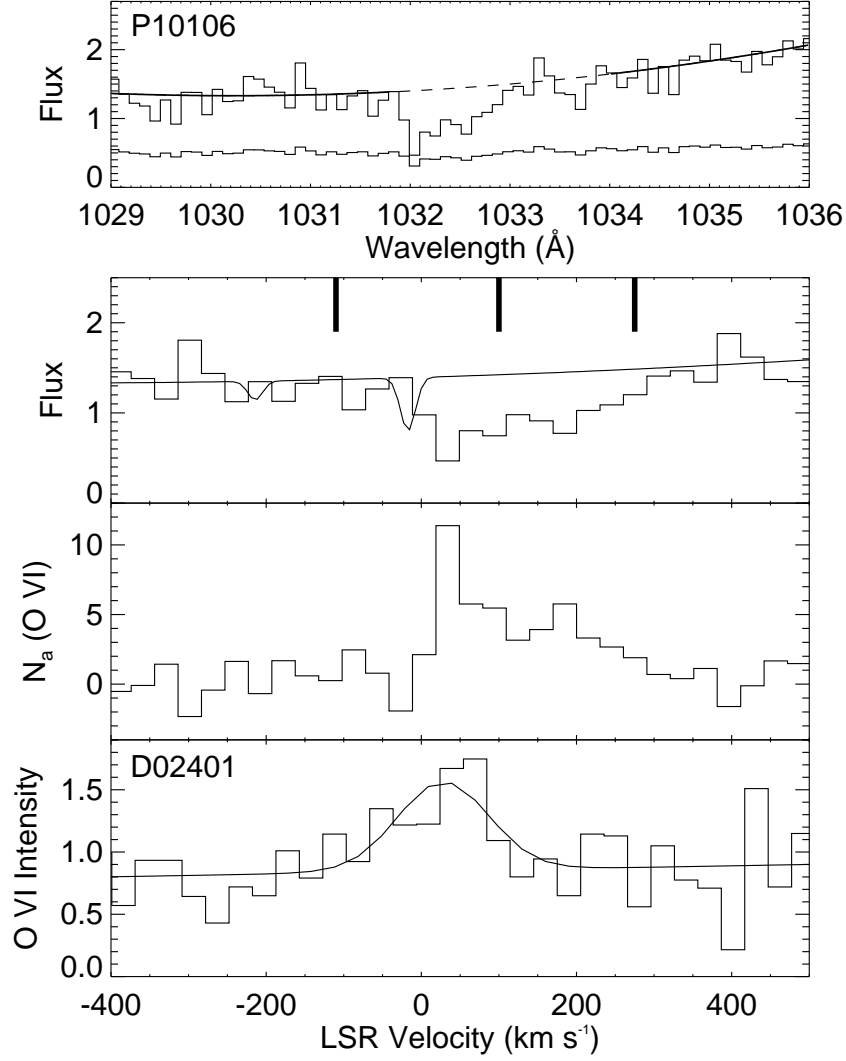
FIG. 7.— *First panel: FUSE* spectrum of Fairall 9 (P10106) showing O VI $\lambda 1032$ absorption from both the Galaxy and the Magellanic Stream. Overplotted are a continuum fit (interpolated over the dashed region) and the error array. Flux units are erg cm^{-2} s^{-1} Å^{-1}. *Second panel:* Spectrum of Fairall 9 plotted as a function of LSR velocity. The spectrum is binned by 8 pixels, or 30 km s^{-1}. The continuum is scaled to account for absorption from the R(3) $\lambda 1031.19$ line of molecular hydrogen (at both low and high velocities). Thick vertical lines mark the limits assumed for the Galactic ($-110 < v < 100$ km s^{-1}) and Magellanic Stream ($100 < v < 275$ km s^{-1}) absorption. *Third panel:* Apparent O VI column density in units of 10^{13} cm^{-2} per velocity bin, computed as described in the text. *Fourth panel:* O VI emission in units of kLU per 30 km s^{-1} velocity bin.
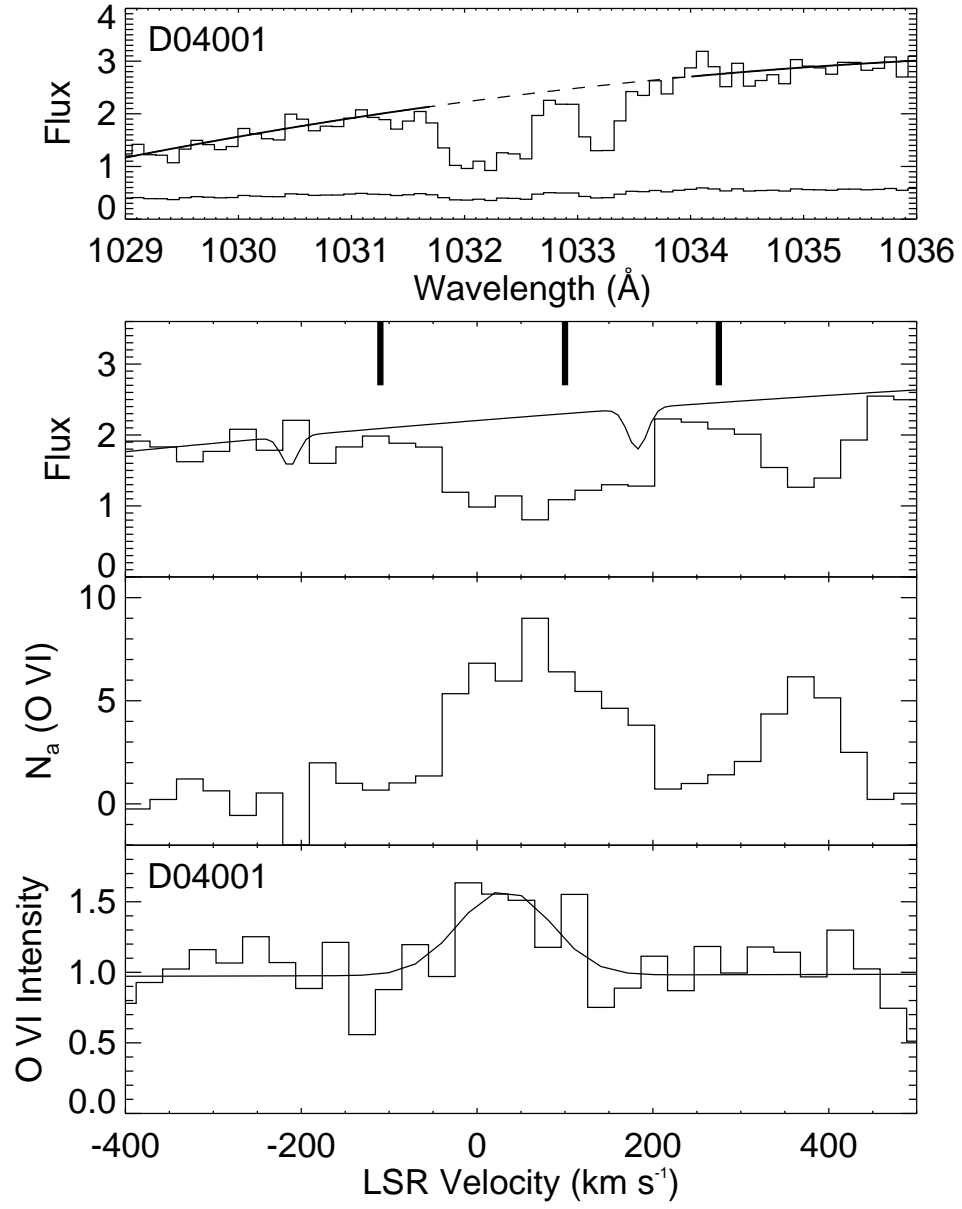
Fig. 8.— Same as Fig. 7, but for NGC 625 (D02401). The O VI emission spectrum is from Paper II.